

Diversity of structural phases in $AGeX_3$ halidesYaorong Luo^{1,2}, Hao Tian^{1,2,3}, Xu Li^{1,2}, Lan Chen^{1,2,*}, Yurong Yang^{1,2,†} and Di Wu^{1,2,‡}¹National Laboratory of Solid State Microstructures and Collaborative Innovation Center of Advanced Microstructures, Department of Materials Science and Engineering, Nanjing University, Nanjing 210093, China²Jiangsu Key Laboratory of Artificial Functional Materials, Nanjing University, Nanjing 210093, China³School of Physics and Electronic Engineering, Zhengzhou Normal University, Zhengzhou 450044, China

(Received 2 May 2022; revised 29 June 2022; accepted 12 July 2022; published 27 July 2022)

Utilizing first-principles and particle swarm optimization methods, we performed a systematic investigation of crystal structural stability and electrical properties of $AGeX_3$ compounds ($A = \text{Li, Na, K, Rb, Cs}$; $X = \text{F, Cl, Br, I}$). Our work not only found the perovskite phases, but also discovered the post-perovskite, post-post-perovskite, and octahedra face-sharing structure phases, which are usually stable under high pressure, large strain, or exist in the inorganic–organic compound. These diverse structural phases provide abundant and promising properties. One striking phase is the $P2_12_12_1$ perovskite in $KGeCl_3$ and $KGeBr_3$, which possesses intrinsic small polar vortices and antivortices that may lead to a gyrotropic phase transition. The ferroelectric phase of $R3c$ (LiGeX_3 , NaGeX_3), $R3m$ (CsGeX_3) and $Pna2_1$ (KGeX_3 , RbGeX_3) were also found. The new $Pna2_1$ phase possesses both proper and hybrid improper polarization, and the latter is evidenced by two original energetic couplings: one coupling polarization with the antipolar distortion from Ge atoms and antipolar distortion from A-site atoms, and another coupling polarization with out-of-phase halide octahedral tilting, in-phase halide octahedral tilting, and antipolar distortion from Ge atoms. The diverse structural phases and electrical properties make Ge-based halide a promising ABX_3 structure family in ferroics and piezoelectrics.

DOI: [10.1103/PhysRevB.106.024112](https://doi.org/10.1103/PhysRevB.106.024112)

I. INTRODUCTION

Perovskite oxides of ABO_3 are widely investigated and have extensive applications in various areas, such as field-effect transistors [1], transducers [2], electrocaloric coolers for computers [3], nonvolatile random-access memory devices, energy storage, and so on [4]. One of the most important and widely investigated properties of ABO_3 is ferroelectricity, which has been investigated for about 100 years. Until now, ferroelectrics is still one of the most interesting research fields, and various new phenomena have recently been discovered, such as the negative capacitance effect [5], polar vortex [6], and polar skyrmion-like structures [7]. Another important property of ABO_3 is multiferroicity, which possesses more than one of the ferroic properties of ferroelectricity, (anti-)ferromagnetism, and ferroelasticity. In the multiferroics ABO_3 , magnetoelectric, magnetoelastic, piezoelectric, elastic–optic, and other interesting effects are discovered due to their more than one of the degree of freedom (charge, lattice, spin, orbitals) [8].

Another perovskites family is halide ABX_3 ($X = \text{F, Cl, Br, and I}$), which has recently attracted considerable scientific attention due to its excellent photovoltaic and optoelectronics [9–11]. The organic–inorganic hybrid halide perovskites such as $\text{CH}_3\text{NH}_3\text{BX}_3$ and $\text{HC}(\text{NH}_2)_2\text{BX}_3$, are usually considered to be the next generation of solar cells, whose power conversion efficiency has achieved 26.4% [12]. Moreover,

a large electrostrictive response [13], ferroelectricity [14], charged domain wall [15], negative thermo-optic coefficient [16], ultralow thermal conductivity, and outstanding thermo-electricity [17] are also revealed in them. For all-inorganic halide perovskites, most studies focus on CsBX_3 ($B = \text{Pb, Sn}$; $X = \text{Cl, Br, and I}$) [11,18–22]. Both CsPbI_3 [20] and CsSnI_3 [22] not only show similar crystal structures and phase-transition behaviors (from $\alpha\text{-Pm}\bar{3}m$ to $\beta\text{-P4/mbm}$ to $\gamma\text{-Pnma}$ and finally to $\sigma\text{-Pnma}$ during the cooling process), but also possess ultralow thermal conductivity [23] and well optoelectronic properties [20,22]. The halide perovskites with Ge atom on the B site also received some scientific attention. Stoumpos *et al.* [24] synthesized the $R3m$ phase of CsGeI_3 and disclosed the large second harmonic generation response in it. Ming *et al.* [25] suggested that CsGeI_3 is a p -type semiconductor and it may be used as an efficient hole transport material in solar cells. However, the electric properties and electronic structure of CsGeI_3 are still unknown. Furthermore, the research on other $AGeX_3$ (A is alkali metal atoms and X is halogen atoms) structures is still lacking, and these structures may exhibit interesting electric and electronic properties.

We combine particle–swarm–optimization (PSO) methods performed by crystal structural predictions software (CALYPSO) and first-principles methods to explore possible crystal structures of candidate Ge-based compounds $AGeX_3$ ($A = \text{Li, Na, K, Rb, and Cs}$; $X = \text{F, Cl, Br, and I}$). The research findings reveal five kinds of ground-state structures and three kinds of ferroelectric perovskites. And then, we perform a comprehensive investigation of the potential application and ferroelectric properties of these structures. We have noticed, most surprisingly, that almost all $AGeX_3$ (except for $X = \text{F}$) compounds could maintain a stable perovskite

*Corresponding author: chenlan@nju.edu.cn

†Corresponding author: yangyr@nju.edu.cn

‡Corresponding author: diwu@nju.edu.cn

TABLE I. The space group of the ground phase of AGeX_3 ($A = \text{Li, Na, K, Rb, Cs}$; $X = \text{F, Cl, Br, I}$). Perovskite (Pv), post-perovskite (pPv), post-post-perovskite (ppPv), and face-sharing (FS) are displayed for characterizing structure.

A-site	X-site			
	F	Cl	Br	I
Li	$P2_1$	pPv- $P\bar{1}$	ppPv- $P1$	ppPv- Pm
Na	$P2_1/c$	pPv- Cc	pPv- Cc	ppPv- $C2/m$
K	pPv- $P2_1/m$	Pv- $P2_12_12_1$	Pv- $P2_12_12_1$	FS- $P2_12_12_1$
Rb	pPv- $P2_1/m$	pPv- $P2_1/m$	Pv- $Pna2_1$	FS- $P2_1/c$
Cs	pPv- $P2_1/m$	Pv- $R3m$	Pv- $R3m$	FS- $Pnma$

structure with ferroelectricity. Moreover, the novel $P2_12_12_1$ phase of KGeCl_3 and KGeBr_3 displays ferroelectric vortices and antivortices, and the $Pna2_1$ phase of KGeX_3 and RbGeX_3 possesses the improper ferroelectricity that origins from new trilinear and quadrilinear energetic couplings. Our findings have significant implications not only for the study of ferroelectric perovskite, but also for the discovery of new potential functional materials.

II. COMPUTATIONAL METHODS

The crystal structural predictions and calculations were performed by the PSO [26] method implemented in the CALYPSO code [27], whose validity and accuracy have been demonstrated in many systems [28–30]. The VIENNA *ab initio* simulation package (VASP) [31–33] was adopted to perform density functional theory (DFT) calculations for relaxing structures and calculating electronic properties of considered AGeX_3 compounds. The projector augmented wave [34,35] pseudopotential and Perdew-Burke-Ernzerhof generalized gradient approximation functional [36] was implemented in the VASP code by explicitly treating three valence electrons for Li ($1s^22s^1$), seven for Na ($2p^63s^1$), nine for K ($3s^23p^64s^1$), nine for Rb ($4s^24p^65s^1$), nine for Cs ($5s^24p^66s^1$), four for Ge ($4s^24p^2$), seven for F ($2s^22p^5$), seven for Cl ($3s^23p^5$), seven for Br ($4s^24p^5$), and seven for I ($5s^25p^5$). The supercell with 20 atoms is used. For a balance of numerical accuracy and computational expense, different cutoffs were used for different compounds: 600 eV for LiGeX_3 ($X = \text{F, Cl, Br, I}$), 500 eV for AGeF_3 ($A = \text{Na, K, Rb, Cs}$), and 380 eV for AGeX_3 ($A = \text{Na, K, Rb, Cs}$; $X = \text{Cl, Br, I}$). The convergence criteria for energy and force were set to 10^{-7} eV and 0.001 eV/Å, respectively. A Monkhorst-Pack k-point mesh of $4 \times 4 \times 4$, $6 \times 6 \times 4$, and $8 \times 8 \times 8$ were used for the 40-atom-cell, 20-atom-cell, and 5-atom-cell cases, respectively. The phonon calculations were carried out by the PHONOPY code [37]. The Berry phase method [38,39] was used for calculating the ferroelectric polarization.

III. RESULTS AND DISCUSSION

We integrated density functional theory and particle-swarm-optimization methods to perform a stability study of 20 kinds of halide perovskite compounds AGeX_3 ($A = \text{Li, Na, K, Rb, Cs}$; $X = \text{F, Cl, Br, I}$). The space group of predicted ground phases is presented in Table I, and ferroelectric per-

ovskite structures (with both ground phases and metastable phases) are presented in Table II. Let us first discuss the ground phase shown in Table I.

A. Ground phases

We can classify the ground phase into five kinds of structures.

(1) *New monoclinic phase.* For LiGeF_3 and NaGeF_3 [see Figs. 1(a) and 1(b)], we found that the lowest energy structure is not a bonded crystal structure, but a molecular-like structure, where three F atoms are bonded to one Ge atom with an F-Ge bond length of 1.89 Å, forming fluorine tetrahedra. The alkali atoms Li or Na are distributed between tetrahedrons, and the space groups of the new structure are $P2_1$ and $P2_1/c$.

(2) *Perovskite (Pv) structure.* The orthorhombic perovskite of the $P2_12_12_1$ phase (Pv- $P2_12_12_1$) is found to be the ground phase for KGeCl_3 and KGeBr_3 [Fig. 1(c)]. This phase possesses chlorine or bromine octahedral rotation and tilting pattern of $a^-a^-c^+$ (Glazer's notation [40]), similar to the common $Pnma$ perovskite structure. Furthermore, the Pv- $P2_12_12_1$ phase is predicted to be the stable structure of epitaxial (-110) BiFeO_3 films under compressive strain, which possesses ferroelectric vortices and antivortices, and its gyrotropic phase transition can be characterized by the appearance of spontaneous optical activity [41,42]. To find the evidence of the ferroelectric vortices and antivortices in Pv- $P2_12_12_1$ of KGeCl_3 and KGeBr_3 , we qualitatively analyze the antiphase displacements of the K atoms by the vector [41]

$$\mathbf{g}_{\mathbf{H},\alpha} = \frac{1}{V} \sum_j Z_{K,\alpha}^* \delta r_{j,\alpha}^K e^{i\mathbf{k}_{\mathbf{H}} \cdot \mathbf{R}_j}, \quad (1)$$

where V is the supercell volume and Z_K^* is the effective charge of K atoms, $\delta r_{j,\alpha}^K$ is the α component of the K atom in the j th five-atom cell, $\mathbf{k}_{\mathbf{H}}$ represents the high symmetry X point (or M point) of the first Brillouin zone of the five-atom cell that corresponds to $\pi/a(0, 0, 1)$ [or $\pi/a(1, 1, 0)$], and \mathbf{R}_j is the position of the Ge atom in the j th five-atom cell. The Cartesian components of $\mathbf{g}_{\mathbf{H}}$ at the X and M points are $\mathbf{g}_{\mathbf{X},\alpha} = -\mathbf{g}_{\mathbf{X},\beta} = 2.99$, $\mathbf{g}_{\mathbf{X},\gamma} = 0$; $\mathbf{g}_{\mathbf{M},\alpha} = \mathbf{g}_{\mathbf{M},\beta} = 0$; and $\mathbf{g}_{\mathbf{M},\gamma} = -5.63$. Figure 2 shows the coexistence of the $\mathbf{g}_{\mathbf{M},\gamma}$ and $\mathbf{g}_{\mathbf{X},\alpha}$ or $\mathbf{g}_{\mathbf{X},\alpha}$ parameters in the Pv- $P2_12_12_1$ phase and then leads to the ferroelectric vortex (blue circle) and antivortex (purple circle). That results are consistent with the case of $P2_12_12_1$ in compressive (-110) BiFeO_3 film. For KGeCl_3 and KGeBr_3 , the Pv- $P2_12_12_1$ phase is the ground state without any strain; gyrotropic phase transition can easily occur in KGeCl_3 and KGeBr_3 , unlike the $P2_12_12_1$ phase in epitaxial (-110) BiFeO_3 films, which only exists at a very large compressive strain (about 7%), which may unstable for most perovskite [41]. Please note that gyrotropic phase transitions are rare in nature, and we are not aware of any gyrotropic phase transition that has ever been reported in any perovskite under ambient conditions. The new Pv- $P2_12_12_1$ phase in KGeCl_3 and KGeBr_3 provides a chance for a gyrotropic phase transition to occur in a pure inorganic perovskite compound, rather than in organic-inorganic compounds [43] and transition-metal dichalcogenides [44]. Compared with the polar vortices and antivortices in $\text{PbTiO}_3/\text{SrTiO}_3$ [6,7], the polar vortices and antivortices in KGeCl_3 and KGeBr_3 are smaller, and also are

TABLE II. Ground states or metastable states of ferroelectric perovskite for $AGeX_3$ ($A = \text{Li, Na, K, Rb, Cs}$; $X = \text{F, Cl, Br, I}$). The space group (s.g.) and its energy (ΔE , millielectron volts/formula unit) respective to the ground phase are shown.

A-site \ X-site	Cl			Br		I	
	F	s.g.	ΔE	s.g.	ΔE	s.g.	ΔE
Li	–	$R3c$	27	$R3c$	50	$R3c$	134
Na	–	$R3c$	23	$R3c$	42	$R3c$	122
K	–	$Pna2_1$	23	$Pna2_1$	5	$Pna2_1$	11
Rb	–	$Pna2_1$	19	$Pna2_1/R3m$	0/60	$Pna2_1/R3m$	23/99
Cs	–	$R3m$	0	$R3m$	0	$R3m$	44

intrinsic, formed by structural symmetry, rather than that seen in $\text{PbTiO}_3/\text{SrTiO}_3$, which is stabilized by structural distortion coupling in interfaces, the depolarization field, and strain [6].

(3) *Post-perovskite (pPv)*. The ground phase of $AGeF_3$ ($A = \text{K, Rb, Cs}$), LiGeCl_3 , NaGeCl_3 , and NaGeBr_3 possess similar structural characteristics: two-dimensional GeX_6 octahedra sheets are formed by sharing edges and corners, alkali

metal cations are distracted between GeX_6 octahedra sheets [see Figs. 1(d)–1(f)]. This kind of ABX_3 with GeX_6 octahedra sheets is the so-called *post-perovskite* [45,46], which has been found under hydrostatic pressure for MgSiO_3 , whose elastic properties well explain the strong seismic anisotropy and anticorrelation between bulk and shear sound velocities in Earth's D'' layer. Note that our calculated symmetry of the

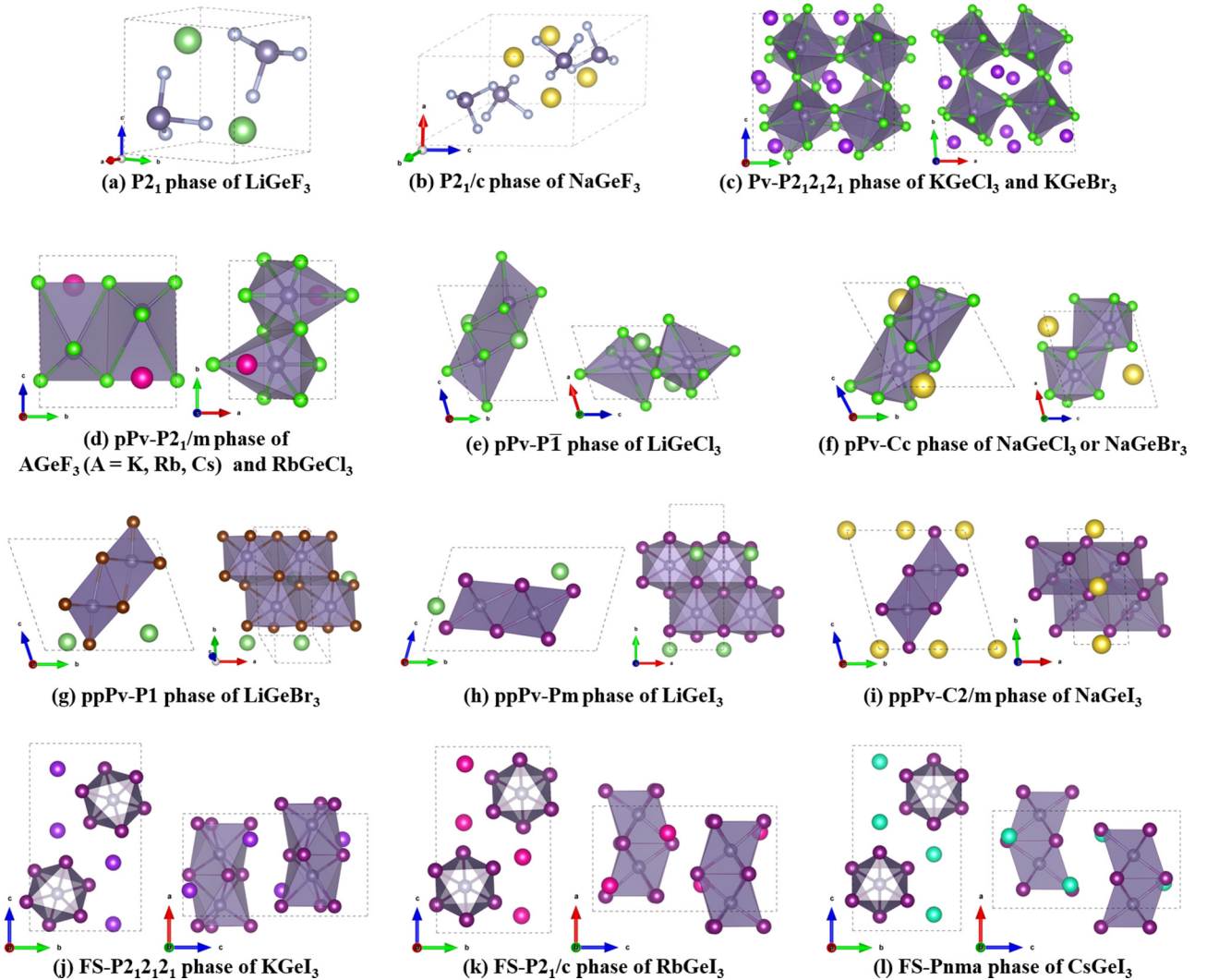


FIG. 1. Structures of ground phase $AGeX_3$ ($A = \text{Li, Na, K, Rb, Cs}$; $X = \text{F, Cl, Br, I}$). (a) and (b) The Ge atoms are connected with F atoms, and the rest is Li or Na. (c)–(l) The X-site atoms (F, Cl, Br, I) occupy the vertices of the octahedra of which the Ge atoms are inside; the rest of the atoms are A-site atoms (Li, Na, K, Rb, Cs). Note that some of lowest energy phases are ferroelectric perovskite structures. We do not present their structures here; they can be found in Fig 3.

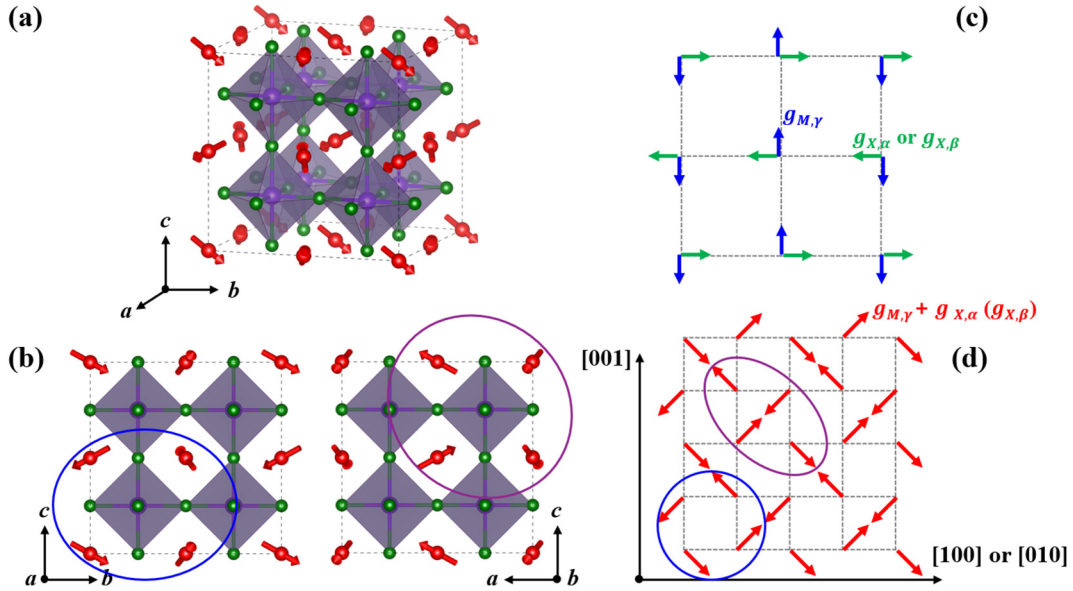


FIG. 2. Vortex and antivortex atomic features of the $P2_12_12_1$ phase of $KGeX_3$ ($X = Cl, Br$). (a) and (b) The K cation movements of the $P2_12_12_1$ phase compared to the cubic structure in different views. (c) and (d) The K cation movements associated with $g_{M,\gamma}$, $g_{X,\alpha}$, and $g_{X,\beta}$, and their sum. The blue and purple circles are used to highlight a ferroelectric vortex and ferroelectric antivortex. Red, purple, and green balls represent the K, Ge, and X (Cl or Br) atoms, respectively.

ppV- $P2_1/m$ phase of $RbGeCl_3$ is in excellent agreement with measurements [47], indicating the accuracy of our calculation and prediction. The ground state of halide *post-perovskite* structures without any pressure provide us with a broad range to find new structures that are different from oxides, where the perovskite is the usual structure.

(4) *Post-post-perovskite (ppPv)*. Another structure family, the so-called *post-post-perovskite* [48,49], is also found to be the ground state for $LiGeBr_3$, $LiGeI_3$, and $NaGeI_3$. In the *post-post-perovskite* structure, one GeX_6 octahedron is connected with four adjacent octahedra by edge sharing, and then the octahedra form a one-dimensional double-chain structural framework in one supercell. Some interesting properties have been found in ppPv- ABO_3 families, including pseudo-Jahn-Teller effects and novel couplings [48], significant piezochromic effects [49], and novel magnetic orderings [50]. Unlike the ppPv- ABO_3 at high hydrostatic pressure, the ppPv phases we predicted at zero hydrostatic pressure may also have some interesting properties.

(5) *Octahedra face-sharing structure*. The ground states of $KGeI_3$, $RbGeI_3$, and $CsGeI_3$ are another different kind of structure in which the BX_6 octahedra are connected by face sharing (FS) and forming octahedra chains [see Figs. 1(j)–1(l)], similar to the $BiNiO_3$ -like hexagonal perovskite structure [51]. This octahedral FS structure is also found in organic-inorganic perovskite [52,53], which gives a giant piezoelectric response. Similarly, this structure is also adopted in the $CsFeCl_3$ system, and it manifests a quantum phase-transition behavior when doped with Rb [54] or when changing the hydrostatic pressure [55]. Fundamentally, these attractive properties or phenomena are not only related to the atomic composition in the compounds, but also are closely related to this unique octahedral FS structure framework. This implies that some other refreshing properties would exist in these new FS phases we found.

B. Ferroelectric properties

From our first-principles and particle-swarm-optimization calculations, some ferroelectric ground states and ferroelectric metastable states with perovskite are discovered. As shown in Table II, $AGeX_3$ ($A = Li, Na, K, Rb, Cs$; $X = Cl, Br, I$) adopts a polar structure with a space group of $R3c$, $R3m$, or $Pna2_1$. Note that the energy difference between the ferroelectric perovskite and ground phase may be different, as shown in Supplemental Material (SM) Table S1 [56] (see also references [57–62] therein). The different calculation results caused by different functionals are usual in DFT calculations [63–66]. On the other hand, the phases considered here are stable or metastable for all the used functional calculations. Their phonon dispersions are also calculated (see SM Fig. S1 [56]) and no imaginary eigenvalues are found for most compounds (except the $R3m$ phase of $RbGeBr_3$ and $RbGeI_3$), hinting at the stability of the polar structures. The $R3m$ phases of $RbGeBr_3$ and $RbGeI_3$ are also shown in Table II as experimental confirmation under some special conditions [60,61], although they have larger energy than that of the $Pna2_1$ phase.

1. The $R3c$ phase

As shown in Table II, $AGeX_3$ ($A = Li, Na$; $X = Cl, Br, I$) possesses the polar perovskite structure where the A site is the light elementary atoms. Note that the cubic, tetragonal, and orthorhombic phases of $LiGeX_3$ [67] and $NaGeX_3$ [68] were studied by first principles [67,68]. The $R3c$ phase for $LiGeX_3$ and $NaGeX_3$ have been missed before, to the best of our knowledge. The structure of the predicted $R3c$ phase is schematized in Fig. 3(a). In this phase, it has antiphase halogen octahedra rotations [antiferrodistortive (AFD)] with an $a^-a^-a^-$ tilt pattern, and features a spontaneous polarization along the [111] pseudocubic direction. The detailed structure parameters are given in SM Table S2 [56]. The lattice constant

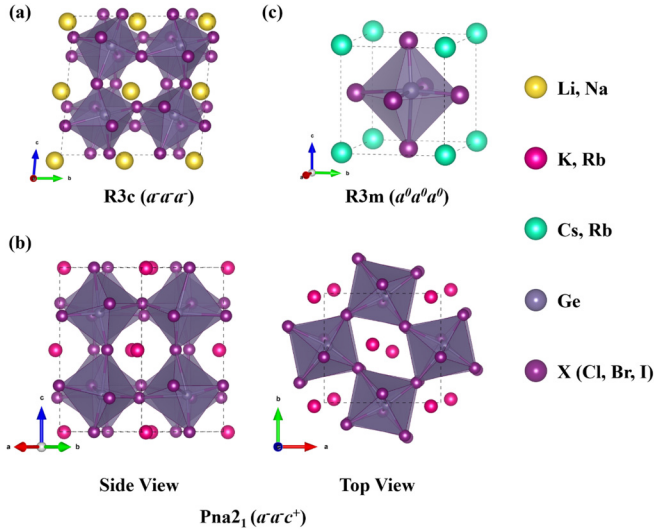


FIG. 3. Crystalline structure of AGeX_3 perovskites studied in this work. (a) $R3c$ phase ($a^- a^- a^-$, No. 161) of AGeX_3 ($A = \text{Li, Na}$; $X = \text{Cl, Br, I}$). (b) $Pna2_1$ phase ($a^- a^- c^+$, No. 33) of AGeX_3 ($A = \text{K, Rb}$; $X = \text{Cl, Br, I}$). (c) $R3m$ phase ($a^0 a^0 a^0$, No. 160) of AGeX_3 ($A = \text{Rb, Cs}$; $X = \text{Cl, Br, I}$).

increases and the angle of octahedral tilting decreases with an increase in the ionic radius of the A -site cation (from Li to Na) or X -site halide anion (from Cl to Br to I). The lattice angle remains nearly identical with different A -site cations and X -site halide anions. The calculated polarizations are between $2.07 \mu\text{C}/\text{cm}^2$ and $12.44 \mu\text{C}/\text{cm}^2$, in which the largest polarization is in NaGeCl_3 and the smallest polarization is in LiGeI_3 [see SM Table S2 [56] and Fig. 4(b)]. The band gap of

the $R3c$ phase is in the range from 1.92 to 3.81 eV (Fig. 4 and SM Table S2 [56]) (note that the band gap is usually underestimated by density functional theory calculations), indicating that all of them are wide-band gap ferroelectric. Very interestingly, the largest band gap and the largest polarization exist in the same compound, which is the long-pursuit material for high-energy density storage in dielectric capacitors. The halide dielectrics may provide a new route for dielectric energy storage. Note that the oxides' ferroelectric $R3c$ phase of BiFeO_3 and LiNbO_3 have large polarizations (70 to $100 \mu\text{C}/\text{cm}^2$) and AFD angles (8° to 14° along the $[111]$ direction) [69,70], but the halide ferroelectric $R3c$ phases possess relatively smaller polarizations ($2.07 \sim 12.44 \mu\text{C}/\text{cm}^2$) and larger AFD angles (14° to 21° along the $[111]$ direction). This difference between oxides and halide ferroelectrics may give different domain structures and properties [71].

2. The $Pna2_1$ phase

As shown in Table II, KGeX_3 and RbGeX_3 ($X = \text{Cl, Br, I}$) possess the $Pna2_1$ phase. They are ground states (RbGeBr_3), or metastable phases with very close energy to ground states (the energy difference is less than 23 meV per f.u.). Note that our predicted $Pna2_1$ phases of RbGeBr_3 and RbGeI_3 are in line with experimental results [60,61]. The calculated $R3m$ phases for RbGeBr_3 and RbGeI_3 are consistent with the high-throughput calculations [72]. Some cubic phases with higher energy than our found $Pna2_1$ and $R3m$ phases are also studied for their promising properties [73–75]. Figure 3(b) shows the structure of the orthorhombic $Pna2_1$ phase, which has a similar AFD pattern of $a^- a^- c^+$ with the $Pnma$ phase (the value of AFD is shown in SM Table S3 [56]), but the $Pna2_1$ phase is a polar structure with a polarization along the $[001]$

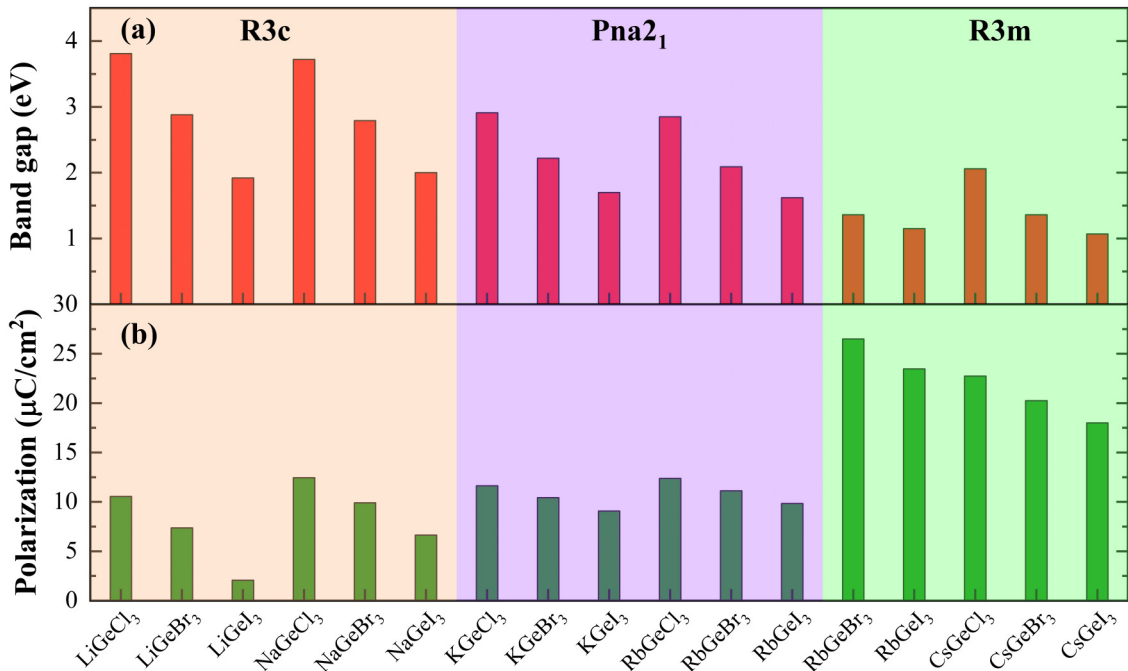


FIG. 4. The band gap (a) and polarization (b) of AGeX_3 perovskites studied in this work. Orange, purple, and green shading represent the $R3c$, $Pna2_1$, and $R3m$ phases of corresponding compounds, respectively. The specific values are shown in SM Tables S2, S3, and S4 [56].

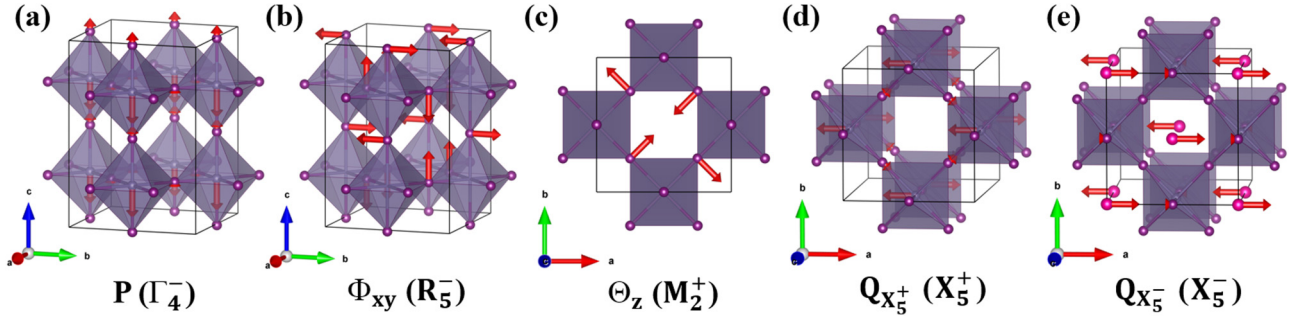


FIG. 5. The five main structural distortion modes of the $Pna2_1$ phase with respect to the high-symmetry reference of the cubic perovskite structure ($Pm\bar{3}m$). (a)–(e) Polar displacement (P , irrep Γ_4^-); out-of-phase, in-plane tilting (Φ_{xy} , irrep R_5^-); in-phase, out-of-plane tilting (Θ_z , irrep M_2^+); antipolar B -site displacements ($Q_{X_5^+}$, irrep X_5^+); and antipolar A -site displacements ($Q_{X_5^-}$, irrep X_5^-), respectively. In (a)–(d), A -site ions are omitted for clarity. Note that the ferroelectric perovskite structure of $AGeX_3$ ($A = K, Rb$; $X = Cl, Br, I$) compounds are all $Pna2_1$ phases. We then use $RbGeI_3$ as an example for our analysis.

direction. The calculated polarization is in the range from 9.07 to 12.37 $\mu C/cm^2$ for $AGeX_3$ ($A = K, Rb$; $X = Cl, Br, I$).

To understand fully the characteristics of the $Pna2_1$ phase, we analyze the structure of $Pna2_1$ with respect to the high-symmetry structure of cubic perovskite (the space group is $Pm\bar{3}m$). As shown in Fig. 5, the $Pna2_1$ phase has five main structural distortion modes: (i) a polar mode where B -site ions move along the $[00\bar{1}]$ direction and X -site atoms move along the $[001]$ direction, generating a polarization along $[001]$ (Γ_4^-); (ii) an out-of-phase, in-plane octahedral tilting mode (Φ_{xy} , irreducible representation R_5^-); (iii) an in-phase, out-of-plane octahedral tilting mode (Θ_z , M_2^+); (iv) an antipolar mode where B -site atoms move along the a or $-a$ direction ($Q_{X_5^+}$, X_5^+); and (v) an antipolar mode where A -site atoms move along the a or $-a$ direction ($Q_{X_5^-}$, X_5^-). Interestingly, from the symmetry analysis (using ISOTROPY [76,77]) these modes can couple with trilinear or quadrilinear forms by

$$E \sim B_1 P_{\Gamma_4^-} Q_{X_5^+} Q_{X_5^-} + B_2 \Phi_{xy} \Theta_z Q_{X_5^-} + B_3 P_{\Gamma_4^-} \Phi_{xy} \Theta_z Q_{X_5^+}, \quad (2)$$

where $P_{\Gamma_4^-}$, $Q_{X_5^+}$, $Q_{X_5^-}$, Φ_{xy} , and Θ_z represent the amplitude of Γ_4^- , X_5^+ , X_5^- , R_5^- , and M_2^+ modes, respectively; and B_1 , B_2 , and B_3 are the parameters of corresponding couplings. The second term of Eq. (2) is the coupling between the in-plane, out-of-phase AFD; out-of-plane, in-phase AFD; and antipolar A -site movements, which usually occur in the structures that possess the $a^-a^-c^+$ AFD pattern [78,79]. The first and third terms of Eq. (2) are trilinear and quadrilinear couplings that include the distortion of polar mode, implying that the polarization is hybrid improper ferroelectricity.

To confirm further the origin of the polarization and verify these couplings, we calculated the dependence of the total energy on the amplitude of distortion. As shown in Fig. 6(a), the X_5^- mode is stable, whereas the $P_{\Gamma_4^-}$, Φ_{xy} , Θ_z , and X_5^+ modes show large instabilities and a large energy gain when their amplitudes are not zero. The polar mode results in a polarization of 8.55 $\mu C/cm^2$. Figure 6(b) shows the energies as a function of the amplitude of $Q_{X_5^-}$ when freezing $P_{\Gamma_4^-}$ and $Q_{X_5^+}$ as well as freezing Φ_{xy} and Θ_z at their amplitude, which leads to the largest energy gain. The two curves in Fig. 6(b) display a single minimum of energy at a nonzero $Q_{X_5^-}$ value, indicating the trilinear couplings of $P_{\Gamma_4^-} Q_{X_5^+} Q_{X_5^-}$ and $\Phi_{xy} \Theta_z Q_{X_5^-}$ of Eq. (2). Note that the energy gain of

$\Phi_{xy} \Theta_z Q_{X_5^-}$ is much larger than that from $P_{\Gamma_4^-} Q_{X_5^+} Q_{X_5^-}$, implying that the parameter B_2 is larger than B_1 . Figure 6(c) displays the energies as a function of the amplitude of P distortion when Φ_{xy} , Θ_z , and $Q_{X_5^+}$ are frozen (green circles) at their amplitude, which leads to the largest energy gain. In contrast to the symmetrical double well of the $P_{\Gamma_4^-}$ mode in Fig. 6(a), the green circles in Fig. 6(c) show an obvious unsymmetrical double well, indicating the energy gain from the quadrilinear coupling $P_{\Gamma_4^-} \Phi_{xy} \Theta_z Q_{X_5^+}$. This quadrilinear coupling implies the hybrid improper polarization also gives a contribution to the polarization, consistent with the fact that the total polarization (9.83 $\mu C/cm^2$) is larger than the proper polarization (8.55 $\mu C/cm^2$). Figure 6(c) also shows the energy as a function of distortion when four distortions of Φ_{xy} , Θ_z , $Q_{X_5^+}$, and $Q_{X_5^-}$ are frozen at their amplitude, which leads to the largest energy gain. Therefore, the couplings in Eq. (2) are all included in the black curve shown in Fig. 6(c), where the energy gain is largest at nonzero P distortion compared with other curves in Fig. 6.

The trilinear and quadrilinear couplings in Eq. (2) between out-of-plane polar, in-plane antipolar, and octahedral tilting distortions can generate a very interesting electric-field response. Under an out-of-plane electric field, the in-plane antipolar distortion of $Q_{X_5^+}$ or $Q_{X_5^-}$ can be switched following the switching of polarization by the coupling $P_{\Gamma_4^-} Q_{X_5^+} Q_{X_5^-}$, which may lead to an unusually large electromechanical response. On the other hand, the octahedral tilting is strongly related to the magnetic easy axis and Dzyaloshinskii–Moriya (DM) interaction [78,80]; the coupling between polarization and octahedral tilting by $P_{\Gamma_4^-} \Phi_{xy} \Theta_z Q_{X_5^+}$ would provide an opportunity for a new magnetoelectric coupling mechanism.

3. The $R3m$ phase

The structure of the $R3m$ phase is schematized in Fig. 3(c), and the lattice parameters are given in SM Table S4 [56]. The calculated lattice constants are in good agreement with experimental and other computational values [60,61,66,81–83]. The $R3m$ phase possesses a polarization along the $[111]$ direction without any octahedral tilting. The polarization is in the range 18 ~ 26.5 $\mu C/cm^2$, which is the largest in the considered halide perovskites of the $R3c$, $Pna2_1$, and $R3m$ phases. The polarization of the $R3m$ phase increases with the increase in the X -site anion radius from I to Cl, similar

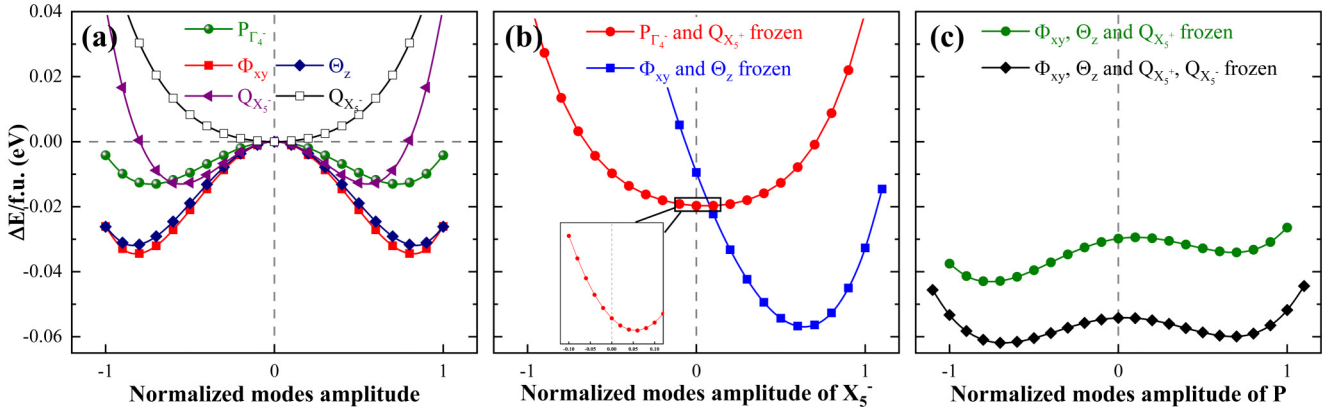


FIG. 6. (a) Energy with respect to the amplitude of the main five structural distortions: P , Φ_{xy} , Θ_z , $Q_{X_5^+}$, and $Q_{X_5^-}$. (b) Energies as a function of the amplitude of $Q_{X_5^-}$ when freezing P and $Q_{X_5^+}$ (red circles), as well as those when freezing Φ_{xy} and Θ_z (blue squares) at their amplitude, which leads to the largest energy gain. (c) Energies as a function of the amplitude of P when Φ_{xy} , Θ_z , and $Q_{X_5^+}$ are frozen (green circles), as well as those when Φ_{xy} , Θ_z , $Q_{X_5^+}$, and $Q_{X_5^-}$ are frozen (black diamonds) at their amplitude, which leads to the largest energy gain. Zero energy is chosen to be the energy of the relaxed $Pm\bar{3}m$ state in all views.

to the $Pna2_1$ and $R3c$ phases. All the $R3m$ phases adopt the semiconducting properties with a band gap from 1.07 ~ 2.06 eV. The band gap is related closely to the X -site anion radius, which increases with decreasing of the X -site radius from I to Cl. The band gap of CsGeX_3 ($X = \text{I, Br, Cl}$) is 1.07 eV, 1.36 eV, and 2.06 eV, respectively (see SM Fig. S2 [56]). The calculated band gaps are in good agreement with previous computational results [24,66,82], but are smaller than the experimental values [24,83] due to the well-known underestimation by density functional theory calculations. Experimentally, CsGeI_3 with a band gap of about 1.60 eV has been synthesized and used for photovoltaic applications [83]. Furthermore, the $R3m$ phase possesses a spontaneous electric polarization that would enhance the desirable separation of charge and concomitant improved carrier lifetimes, and cause an above-band gap voltage [84,85]. These results suggest that CsGeI_3 may be a good ferroelectric photovoltaics material, which is worthy of further investigation.

C. Discussion

Ferroelectric perovskites of Ge-based halide are found in our calculations. Let us discuss the mechanism of forming the halide perovskite structure and compare that with oxide perovskite. The tolerance factor (t) and octahedral factor (μ) are important factors for forming the perovskite structure, which is defined by

$$t = \frac{r_A + r_X}{\sqrt{2}(r_B + r_X)} \quad (3)$$

and

$$\mu = \frac{r_B}{r_X}, \quad (4)$$

where r_A , r_B , and r_X are ionic radii of the A site, B site, and X site, respectively. The tolerance factor and octahedral factor map is displayed in Fig. 7 and the detailed values are in SM Table S5 [56].

It is clear that the μ of Ge-based halide perovskites (except for $X = \text{F}$; AGeF_3 is nonperovskite) are all lower than 0.41 and far lower than that of Pb-based and Sn-based perovskites. The elements Ge, Sn, and Pb belong to the same main group,

but with different ionic radii. The small ionic radii of Ge would result in a small μ . Moreover, Ge- X bonds possess stronger covalent hybridization than others; hence, Ge-based perovskites possess ferroelectricity more easily.

The tolerance factor, for Ge-based perovskites has been calculated to be in the range of 0.80 to 1.06 (except for CsGeF_3). In general, the tolerance factor could assess whether the A -site cation can fit within the space between the corner-sharing BX_6 octahedron [86]. As shown in Fig. 7, when $t < 0.9$, the AGeX_3 ($A = \text{Li, Na}$) perovskite structure is the $R3c$ phase with an $a^-a^-a^-$ octahedral tilting; when $0.9 < t < 0.95$, the AGeX_3 ($A = \text{K, Rb}$) perovskite structure is the $Pna2_1$ phase with an $a^-a^-c^+$ octahedral tilting; and when $t > 0.95$, the AGeX_3 ($A = \text{Rb, Cs}$) perovskite structure is the $R3m$ phase without any octahedral tilting. This is similar to the oxide perovskite, where the structures with a large tolerance factor would present a cubic structure while the structures with a small tolerance factor possess octahedral tilting in the orthorhombic or rhombohedral crystal structure [57,58,86,87]. For the very small t factor or very large t factor in Fig. 7, no perovskite structure is found, which is similar to the inorganic-organic hybrid halide perovskites [88]. The octahedral factor in halide perovskite ($0.3 < \mu < 0.7$) is smaller than oxide perovskite ($0.41 < t < 1.06$), as r_X is larger than r_O . This difference of μ between halides and oxides leads to the experience of determining the perovskite structure in oxides does not work in halides.

The novel phases—including $P2_12_12_1$ perovskite, post-perovskite, and post-post-perovskite—are found in AGeX_3 under ambient conditions from our calculations. However, perovskite oxides do not possess these phases under ambient conditions. This difference can be explained by three factors. First, the electronegativity of chloride (3.16), bromide (2.96), and iodide (2.66) is smaller than oxygen (3.44), which results in a change in interatomic distance due to the covalence effects [62]. Second, the divalent oxygen ions have twice the nominal charge of halogen ions and therefore lead to large Coulomb interactions [89]. Third, the ionic radius of Cl, Br, and I ions are larger than O, and the Ge ionic radii are also

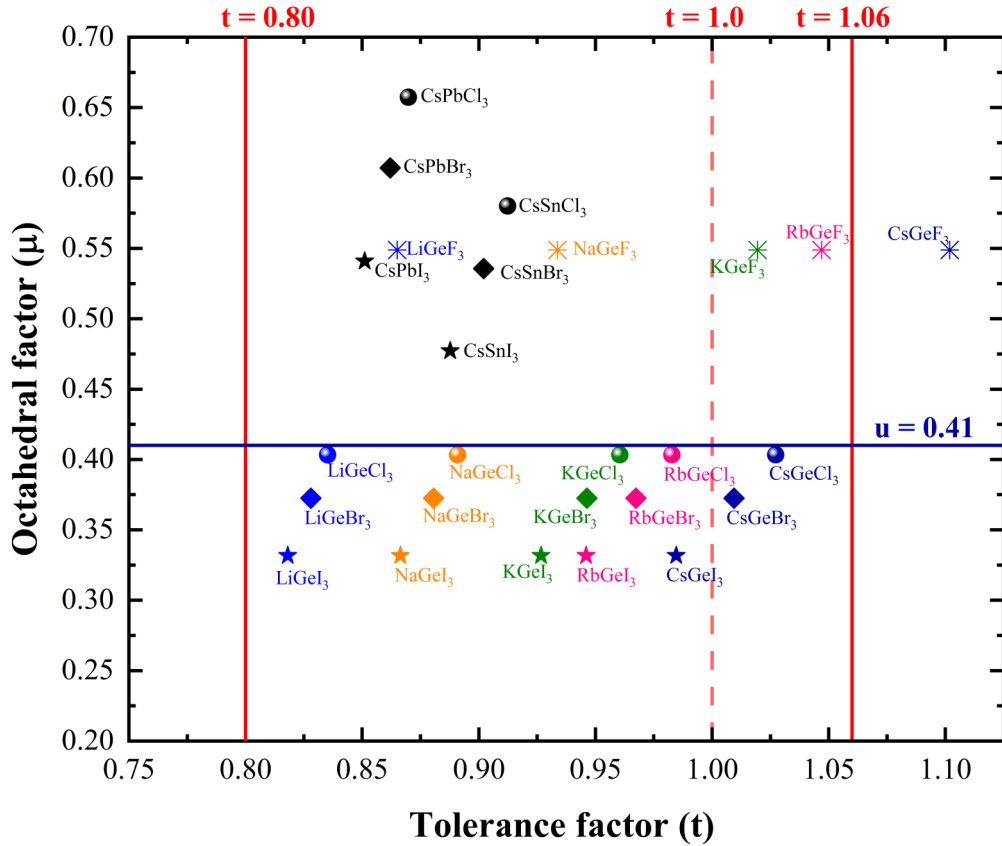


FIG. 7. The tolerance factor (t) and octahedral factor (μ) structure map of $AGeX_3$, $CsSnX_3$, and $CsPbX_3$ (see SM Table S5 [56] for detailed calculations and ionic radii). Empirically, $0.80 < t < 1.06$ (red solid lines) is usually used to evaluate the formation of the perovskite structure. Note: $AGeF_3$ is nonperovskite.

larger than the B -site $3d$ -transition metal atoms in ABO_3 oxides [62]. These three factors may lead to the formation of new phases, such as $P2_12_12_1$ perovskite, post-perovskite, and post-post-perovskite, which are stable in $AGeX_3$ at ambient conditions, whereas they are only stable in oxides under large compressive strains and pressures [41,48–50].

IV. SUMMARY

In summary, we investigated the crystal structural stability and electrical properties of Ge halide perovskite $AGeX_3$ by utilizing the particle–swarm–optimization and first-principles methods. The ground-state pPv and ppPv we obtained are at zero hydrostatic pressure, which is different from the case of ABO_3 at high hydrostatic pressure, and they may have some interesting properties. An octahedral face-sharing structure was considered to be the ground state for $KGeI_3$, $RbGeI_3$, and $CsGeI_3$. For $KGeCl_3$ and $KGeBr_3$, the ground state is the Pv- $P2_12_12_1$ phase, which carries ferroelectric vortices and antivortices. Besides, a new series of robust ferroelectric perovskite compounds have been found: (i) the $R3c$ phase of $AGeX_3$ ($A = Li, Na; X = Cl, Br, I$), (ii) the $Pna2_1$ phase of $AGeX_3$ ($A = K, Rb; X = Cl, Br, I$), and (iii) the $R3m$ phase of $CsGeX_3$ ($X = Cl, Br, I$). For the same crystal symmetry, both polarization and band gap increase with decreasing the

X -site ionic radius from I to Br to Cl. The polarization of the $Pna2_1$ phase consists of two parts: proper polarization and hybrid improper polarization. The former derives from the polarization mode; the latter derives from the results of two energetic couplings: (i) a trilinear coupling (polarization with A -site and B -site antipolarization) and (ii) a quadrilinear coupling (polarization with out-of-phase and in-phase GeX_6 octahedral tilting and B -site antipolarization). In a word, our current findings reveal a suite of new, striking structures that will help guide computer simulation and experimental synthesis in material screening and will enrich the perovskite family of inorganic halide.

ACKNOWLEDGMENTS

The authors thank the National Science Foundation of China (Grants No. 11874207, No. 51725203, No. 51721001, No. 52003117, No. 12104416, and No. U1932115), the National Key R&D Program of China (Grant No. 2020YFA0711504), and the Natural Science Foundation of Jiangsu Province (Grant No. BK20200262). They are grateful to the program for innovative talents and entrepreneur in Jiangsu (JSSCTD202101) and the HPCC resources of Nanjing University for the calculations.

- [1] S. Mathews, R. Ramesh, T. Venkatesan, and J. Benedetto, *Science* **276**, 238 (1997).
- [2] F. Li, M. J. Cabral, B. Xu, Z. Cheng, E. C. Dickey, J. M. LeBeau, J. Wang, J. Luo, S. Taylor, W. Hackenberger, L. Bellaiche, Z. Xu, L.-Q. Chen, T. R. Shrout, and S. Zhang, *Science* **364**, 264 (2019).
- [3] J. F. Scott, *Science* **315**, 954 (2007).
- [4] S. Li, Z. Zhao, J. Zhao, Z. Zhang, X. Li, and J. Zhang, *ACS Appl. Nano Mater.* **3**, 1063 (2020).
- [5] A. K. Yadav, K. X. Nguyen, Z. Hong, P. Garcia-Fernandez, P. Aguado-Puente, C. T. Nelson, S. Das, B. Prasad, D. Kwon, S. Cheema, A. I. Khan, C. Hu, J. Iniguez, J. Junquera, L.-Q. Chen, D. A. Muller, R. Ramesh, and S. Salahuddin, *Nature (London)* **565**, 468 (2019).
- [6] A. K. Yadav, C. T. Nelson, S. L. Hsu, Z. Hong, J. D. Clarkson, C. M. Schlepueetz, A. R. Damodaran, P. Shafer, E. Arenholz, L. R. Dedon, D. Chen, A. Vishwanath, A. M. Minor, L. Q. Chen, J. F. Scott, L. W. Martin, and R. Ramesh, *Nature (London)* **530**, 198 (2016).
- [7] L. Han *et al.*, *Nature (London)* **603**, 63 (2022).
- [8] J. Zhang and R. D. Averitt, *Annu. Rev. Mater. Res.* **44**, 19 (2014).
- [9] H. Zhou, Q. Chen, G. Li, S. Luo, T.-b. Song, H.-S. Duan, Z. Hong, J. You, Y. Liu, and Y. Yang, *Science* **345**, 542 (2014).
- [10] S. Meloni, T. Moehl, W. Tress, M. Franckevicius, M. Saliba, Y. H. Lee, P. Gao, M. K. Nazeeruddin, S. M. Zakeeruddin, U. Rothlisberger, and M. Graetzel, *Nat. Commun.* **7**, 10334 (2016).
- [11] K. P. Marshall, M. Walker, R. I. Walton, and R. A. Hatton, *Nat. Energy* **1**, 16178 (2016).
- [12] R. Lin, J. Xu, M. Wei, Y. Wang, Z. Qin, Z. Liu, J. Wu, K. Xiao, B. Chen, S. M. Park, G. Chen, H. R. Atapattu, K. R. Graham, J. Xu, J. Zhu, L. Li, C. Zhang, E. H. Sargent, and H. Tan, *Nature (London)* **603**, 73 (2022).
- [13] B. Chen, T. Li, Q. Dong, E. Mosconi, J. Song, Z. Chen, Y. Deng, Y. Liu, S. Ducharme, A. Gruverman, F. De Angelis, and J. Huang, *Nat. Mater.* **17**, 1020 (2018).
- [14] A. D. Schulz, H. Roehm, T. Leonhard, S. Wagner, M. J. Hoffmann, and A. Colmann, *Nat. Mater.* **18**, 1050 (2019).
- [15] L. Chen, C. Paillard, H. J. Zhao, J. Iniguez, Y. R. Yang, and L. Bellaiche, *NPJ Comput. Mater.* **4**, 75 (2018).
- [16] T. Handa, H. Tahara, T. Aharen, A. Shimazaki, A. Wakamiya, and Y. Kanemitsu, *Phys. Rev. Materials* **4**, 074604 (2020).
- [17] S. Hu, Z. Ren, A. B. Djurisc, and A. L. Rogach, *ACS Energy Lett.* **6**, 3882 (2021).
- [18] R. Prasanna, A. Gold-Parker, T. Leijtens, B. Conings, A. Babayigit, H.-G. Boyen, M. F. Toney, and M. D. McGehee, *J. Am. Chem. Soc.* **139**, 11117 (2017).
- [19] J. Liang, C. Wang, Y. Wang, Z. Xu, Z. Lu, Y. Ma, H. Zhu, Y. Hu, C. Xiao, X. Yi, G. Zhu, H. Lv, L. Ma, T. Chen, Z. Tie, Z. Jin, and J. Liu, *J. Am. Chem. Soc.* **138**, 15829 (2016).
- [20] J. A. Steele *et al.*, *Science* **365**, 679 (2019).
- [21] D. H. Fabini, G. Laurita, J. S. Bechtel, C. C. Stoumpos, H. A. Evans, A. G. Kontos, Y. S. Raptis, P. Falaras, A. Van der Ven, M. G. Kanatzidis, and R. Seshadri, *J. Am. Chem. Soc.* **138**, 11820 (2016).
- [22] I. Chung, J.-H. Song, J. Im, J. Androulakis, C. D. Malliakas, H. Li, A. J. Freeman, J. T. Kenney, and M. G. Kanatzidis, *J. Am. Chem. Soc.* **134**, 8579 (2012).
- [23] W. Lee, H. Li, A. B. Wong, D. Zhang, M. Lai, Y. Yu, Q. Kong, E. Lin, J. J. Urban, J. C. Grossman, and P. Yang, *Proc. Natl. Acad. Sci. USA* **114**, 8693 (2017).
- [24] C. C. Stoumpos, L. Frazer, D. J. Clark, Y. S. Kim, S. H. Rhim, A. J. Freeman, J. B. Ketterson, J. I. Jang, and M. G. Kanatzidis, *J. Am. Chem. Soc.* **137**, 6804 (2015).
- [25] W. Ming, H. Shi, and M.-H. Du, *J. Mater. Chem. A* **4**, 13852 (2016).
- [26] Y. Wang, J. Lv, L. Zhu, and Y. Ma, *Phys. Rev. B* **82**, 094116 (2010).
- [27] Y. Wang, J. Lv, L. Zhu, and Y. Ma, *Comput. Phys. Commun.* **183**, 2063 (2012).
- [28] C. Liu, W. Wan, J. Ma, W. Guo, and Y. Yao, *Nanoscale* **10**, 7984 (2018).
- [29] Y. Huang, Z. Hu, K. Li, and X. Shao, *Comp. Mater. Sci.* **143**, 403 (2018).
- [30] S. Lu, Y. Wang, H. Liu, M.-s. Miao, and Y. Ma, *Nat. Commun.* **5**, 3666 (2014).
- [31] G. Kresse and J. Furthmuller, *Phys. Rev. B* **54**, 11169 (1996).
- [32] G. Kresse and J. Furthmuller, *Comp. Mater. Sci.* **6**, 15 (1996).
- [33] G. Kresse and J. Hafner, *Phys. Rev. B* **47**, 558 (1993).
- [34] G. Kresse and D. Joubert, *Phys. Rev. B* **59**, 1758 (1999).
- [35] P. E. Blochl, *Phys. Rev. B* **50**, 17953 (1994).
- [36] J. P. Perdew, K. Burke, and M. Ernzerhof, *Phys. Rev. Lett.* **77**, 3865 (1996).
- [37] A. Togo, and I. Tanaka, *Scripta Mater.* **108**, 1 (2015).
- [38] N. A. Spaldin, *J. Solid State Chem.* **195**, 2 (2012).
- [39] R. D. King-Smith and D. Vanderbilt, *Phys. Rev. B* **47**, 1651 (1993).
- [40] A. M. Glazer, *Acta Crystallogr. Sect. B* **28**, 3384 (1972).
- [41] S. Prosandeev, I. A. Kornev, and L. Bellaiche, *Phys. Rev. Lett.* **107**, 117602 (2011).
- [42] S. V. Akimov and E. F. Dudnik, *Phys. Solid State* **51**, 1420 (2009).
- [43] A. Gomez Cuevas, J. M. Perez Mato, M. J. Tello, G. Madariaga, J. Fernandez, L. Echarri, F. J. Zuniga, and G. Chapuis, *Phys. Rev. B* **29**, 2655 (1984).
- [44] S.-Y. Xu, Q. Ma, Y. Gao, A. Kogar, A. Zong, A. M. Mier Valdivia, T. H. Dinh, S.-M. Huang, B. Singh, C.-H. Hsu, T.-R. Chang, J. P. C. Ruff, K. Watanabe, T. Taniguchi, H. Lin, G. Karapetrov, D. Xiao, P. Jarillo-Herrero, and N. Gedik, *Nature (London)* **578**, 545 (2020).
- [45] M. Murakami, K. Hirose, K. Kawamura, N. Sata, and Y. Ohishi, *Science* **304**, 855 (2004).
- [46] A. R. Oganov and S. Ono, *Nature (London)* **430**, 445 (2004).
- [47] D. Messer, *Z. Naturforsch. B* **33**, 366 (1978).
- [48] C. Xu, Y. Li, B. Xu, J. Iniguez, W. Duan, and L. Bellaiche, *Adv. Funct. Mater.* **27**, 1604513 (2017).
- [49] H. Tian, X. Y. Kuang, A. J. Mao, Y. R. Yang, C. S. Xu, S. O. Sayedaghaee, and L. Bellaiche, *Phys. Rev. B* **97**, 020103(R) (2018).
- [50] C. Xu, B. Xu, Y. Yang, H. Dong, A. R. Oganov, S. Wang, W. Duan, B. Gu, and L. Bellaiche, *Phys. Rev. B* **91**, 020101(R) (2015).
- [51] J. Lander, *Acta Crystallogr.* **4**, 148 (1951).
- [52] Y.-M. You, W.-Q. Liao, D. Zhao, H.-Y. Ye, Y. Zhang, Q. Zhou, X. Niu, J. Wang, P.-F. Li, D.-W. Fu, Z. Wang, S. Gao, K. Yang, J.-M. Liu, J. Li, Y. Yan, and R.-G. Xiong, *Science* **357**, 306 (2017).

- [53] W.- Q. Liao, D. Zhao, Y.- Y. Tang, Y. Zhang, P.- F. Li, P.- P. Shi, X.- G. Chen, Y.- M. You, and R.- G. Xiong, *Science* **363**, 1206 (2019).
- [54] S. Hayashida, L. Stoppel, Z. Yan, S. Gvasaliya, A. Podlesnyak, and A. Zheludev, *Phys. Rev. B* **99**, 224420 (2019).
- [55] S. Hayashida, O. Zaharko, N. Kurita, H. Tanaka, M. Hagihala, M. Soda, S. Itoh, Y. Uwatoko, and T. Masuda, *Phys. Rev. B* **97**, 140405(R) (2018).
- [56] See Supplemental Material at <http://link.aps.org/supplemental/10.1103/PhysRevB.106.024112> for details of the phonon dispersion curves, lattice parameters, polarization, and band gap.
- [57] R. Ouyang, *Chem. Mater.* **32**, 595 (2020).
- [58] C. J. Bartel, C. Sutton, B. R. Goldsmith, R. H. Ouyang, C. B. Musgrave, L. M. Ghiringhelli, and M. Scheffler, *Sci. Adv.* **5**, eaav0693 (2019).
- [59] Q. Sun and W.- J. Yin, *J. Am. Chem. Soc.* **139**, 14905 (2017).
- [60] G. Thiele, H. W. Rotter, and K. D. Schmidt, *Z. Anorg. Allg. Chem.* **571**, 60 (1989).
- [61] G. Thiele, H. W. Rotter, and K. D. Schmidt, *Z. Anorg. Allg. Chem.* **559**, 7 (1988).
- [62] R. D. Shannon, *Acta Crystallogr. Sect. A* **32**, 751 (1976).
- [63] Y. Yang, B. Xu, C. Xu, W. Ren, and L. Bellaiche, *Phys. Rev. B* **97**, 174106 (2018).
- [64] O. Diéguez, O. E. González-Vázquez, J. C. Wojdeł, and J. Íñiguez, *Phys. Rev. B* **83**, 094105 (2011).
- [65] H. Aramberri, C. Cazorla, M. Stengel, and J. Iniguez, *npj Comput. Mater.* **7**, 196 (2021).
- [66] G. Walters and E. H. Sargent, *J. Phys. Chem. Lett.* **9**, 1018 (2018).
- [67] N. A. Abdulkareem, B. M. Ilyas, and S. A. Sami, *Mater. Sci. Semicond. Process.* **131**, 105858 (2021).
- [68] X. Mao, L. Sun, T. Wu, T. Chu, W. Deng, and K. Han, *J. Phys. Chem. C* **122**, 7670 (2018).
- [69] J. B. Neaton, C. Ederer, U. V. Waghmare, N. A. Spaldin, and K. M. Rabe, *Phys. Rev. B* **71**, 014113 (2005).
- [70] D. Lee, R. K. Behera, P. Wu, H. Xu, Y. L. Li, S. B. Sinnott, S. R. Phillpot, L. Q. Chen, and V. Gopalan, *Phys. Rev. B* **80**, 149904(E) (2009).
- [71] G. F. Nataf, M. Guennou, J. M. Gregg, D. Meier, J. Hlinka, E. K. H. Salje, and J. Kreisel, *Nat. Rev. Phys.* **2**, 634 (2020).
- [72] S. Koerbel, M. A. L. Marques, and S. Botti, *J. Mater. Chem. C* **4**, 3157 (2016).
- [73] I. Hamideddine, N. Tahiri, O. El Bounagui, and H. Ez-Zahraouy, *J. Korean Ceram. Soc.* **59**, 350 (2022).
- [74] S. Wang, M. Huang, Y.- N. Wu, and S. Chen, *Adv. Theory Simul.* **4**, 2100060 (2021).
- [75] M. Houari, B. Bouadjemi, S. Haid, M. Matougui, T. Lantri, Z. Aziz, S. Bentata, and B. Bouhaf, *Indian J. Phys.* **94**, 455 (2020).
- [76] B. J. Campbell, H. T. Stokes, D. E. Tanner, and D. M. Hatch, *J. Appl. Crystallogr.* **39**, 607 (2006).
- [77] D. M. Hatch and H. T. Stokes, *J. Appl. Crystallogr.* **36**, 951 (2003).
- [78] L. Chen, C. S. Xu, H. Tian, H. J. Xiang, J. Iniguez, Y. R. Yang, and L. Bellaiche, *Phys. Rev. Lett.* **122**, 247701 (2019).
- [79] H. J. Zhao, W. Ren, Y. R. Yang, J. Iniguez, X. M. Chen, and L. Bellaiche, *Nat. Commun.* **5**, 4021 (2014).
- [80] J. T. Heron, J. L. Bosse, Q. He, Y. Gao, M. Trassin, L. Ye, J. D. Clarkson, C. Wang, J. Liu, S. Salahuddin, D. C. Ralph, D. G. Schlom, J. Iniguez, B. D. Huey, and R. Ramesh, *Nature (London)* **516**, 370 (2014).
- [81] G. Thiele, H. W. Rotter, and K. D. Schmidt, *Z. Anorg. Allg. Chem.* **545**, 148 (1987).
- [82] U.- G. Jong, C.- J. Yu, Y.- H. Kye, Y.- G. Choe, W. Hao, and S. Li, *Inorg. Chem.* **58**, 4134 (2019).
- [83] T. Krishnamoorthy, H. Ding, C. Yan, W. L. Leong, T. Baikie, Z. Zhang, M. Sherburne, S. Li, M. Asta, N. Mathews, and S. G. Mhaisalkar, *J. Mater. Chem. A* **3**, 23829 (2015).
- [84] J. M. Frost, K. T. Butler, F. Brivio, C. H. Hendon, M. van Schilfgaarde, and A. Walsh, *Nano Lett.* **14**, 2584 (2014).
- [85] I. Grinberg, D. V. West, M. Torres, G. Gou, D. M. Stein, L. Wu, G. Chen, E. M. Gallo, A. R. Akbashev, P. K. Davies, J. E. Spanier, and A. M. Rappe, *Nature (London)* **503**, 509 (2013).
- [86] W. Travis, E. N. K. Glover, H. Bronstein, D. O. Scanlon, and R. G. Palgrave, *Chem. Sci.* **7**, 4548 (2016).
- [87] J. Ignacio Uribe, D. Ramirez, J. Mario Osorio-Guillen, J. Osorio, and F. Jaramillo, *J. Phys. Chem. C* **120**, 16393 (2016).
- [88] Z. Li, M. Yang, J.- S. Park, S.- H. Wei, J. J. Berry, and K. Zhu, *Chem. Mater.* **28**, 284 (2016).
- [89] M.- H. Du and D. J. Singh, *Phys. Rev. B* **82**, 045203 (2010).